MANIFESTATION OF MESOSPHERIC BORES IN THE NIGHTGLOW OVER YAKUTIA

©2025 O.V. Tyschuk*, I.I. Koltovskoy**, S.V. Nikolashkin***

Yu.G. Shafer Institute of Cosmophysical Research and Aeronomy SB RAS (IKFIA SB RAS), Yakutsk, Russia

*e-mail: oleSmile@mail.ru

**e-mail: koltik@ikfia.ysn.ru

***e-mail: nikolashkin@ikfia.ysn.ru

Received April 08, 2024

Revised October 11, 2024

Accepted for publication December 12, 2024

The article describes two cases of observation of mesospheric bores, which are prominent wave fronts observed using night airglow data recorded by all-sky cameras over the central part of Yakutia (northeastern Siberia). The purpose of the work is to study the peculiarities of propagation and formation mechanism of this phenomenon. In the first case, the manifestation of a bore in the emissions of hydroxyl OH molecules at the level of the mesopause (altitude 87 km) and the green line of atomic oxygen [OI] (altitude 97 km) is described. In the second case, a description of a bore recorded in the emission of hydroxyl OH molecules is presented. The wavelength, phase velocity of propagation, wave period, direction of propagation, time and duration of the phenomenon, are calculated. Possible sources of formation of the mesospheric bore are also discussed.

DOI: 10.31857/S00167940250309e9

1. INTRODUCTION

Atmospheric waves play an important role in the dynamics of the mesosphere and lower thermosphere. Understanding the mechanisms of air mass movement is very important and remains a relevant task in the era of global climate change. Among common wave disturbances in the mesosphere, the manifestation of a distinctive solitary wave can occasionally be observed. This phenomenon represents a clear wave front that separates a part of space already involved in the wave process from an area where oscillations have not yet occurred [Saveliev, 1970]. This wave process was named the mesospheric bore, which comes from the Old Norse "bara" and translates as " wave, ripple " [Tricker, 1969]. The mesospheric bore, representing an intensification of

atmospheric gravity waves, can affect momentum and energy fluxes and thereby influence the thermal regime and composition at all atmospheric levels.

The first mention of bore in the airglow of the night sky was made by Taylor et al. [1995] who described it as " an exciting gravity wave event " observed over the Haleakala volcano crater (USA) during the Airborne Lidar and Observations of Hawaiian Airglow campaign (ALOHA-93). Images obtained using an all-sky camera in the hydroxyl OH molecular emission airglow revealed a band in the form of a linear front, followed by a field of increased brightness across the entire sky. The speed of this front was determined to be 76 m/s. Behind the front, a manifestation of a wave periodic structure in the form of bands of maximum and minimum airglow intensity was clearly noticeable. These waves moved at the speed of the front and were bound to it. The same was observed in three other atmospheric airglow layers arising from Na at an altitude of ~90 km (resonance doublet), O_2 at an altitude of ~94 km (atmospheric bands), and [OI] at an altitude of ~96 km (green line). The authors noted an interesting effect: while the two lower airglow layers, OH and Na, demonstrated an enhancement in the brightness of the front and its subsequent wave field, the two upper airglow layers, O_2 and [OI], demonstrated the opposite effect. In other words, the images of OH and Na airglow were like " negative photographs " for the images of O_2 and [OI] airglow. This same effect was confirmed in an event that occurred on February 2, 2003, over Australia in the OH and O_2 emission airglow layers [Walterscheid et al., 2012].

Along with the analysis of the glow brightness from all-sky camera images, the temperature from the OH layer was studied using a ground-based interferometer [Taylor et al., 1995]. A smooth change in the average temperature was observed, followed by a sudden jump after ~15 minutes. This jump coincided with the passage of a bore at the zenith, where the interferometer was directed. By analogy with the bore phenomenon in the River Mersey [Tricker, 1969], it was suggested that the wave front in the night sky airglow was caused by strong tidal flow in the mesosphere. Based on this, it was shown that there exists a horizontal waveguide channel located midway between the maxima of the Na and O_2 layers (at altitudes between 90 and 94 km) through which the bore propagated. At that moment, the lower OH and Na layers descended (becoming warmer, denser, and brighter), while the upper O_2 and [OI] layers were symmetrically vertically shifted upward (becoming colder, less dense, and less bright). This layer structure is called mesospheric inversion layers (MIL).

Dewan and Picard [2001] explained the mechanism of mesospheric bore formation by analogy with the theory of river bore generation described by Stoker [1948]. In MIL, something like an accelerating " piston " begins to form a wave. As the wave amplitude increases, the speed of the

wave crest (peak) proportionally increases relative to the wave base (foundation). At some point in time, the steepness of the wave reaches its critical value and the slope of the wave front becomes vertical. However, the wave crest does not break in the mesosphere, resulting in the formation of a mesospheric bore. The authors calculated that the formation of a mesospheric bore occurs over approximately 12 hours, of which 4 hours are spent on accelerating the " piston " in the MIL and 8 hours on reaching the critical value of wave steepness. The role of the " piston " is probably performed by the mesospheric tide – the interaction of internal gravity waves (IGW) from powerful sources with a critical layer. The critical layer blocks the vertical propagation of IGW by the mean zonal wind flow (the speed of the zonal background wind coincides with the phase velocity of the IGW).

The generalization of all basic theory about bores allowed formulating the following criteria for identifying mesospheric bores [Loughmiller et al., 2007]:

1) presence of a mesospheric inversion layer MIL;
2) period of increased activity of wave disturbances, internal gravitational waves;
3) the wave front separates the atmospheric airglow into bright and dark regions;
4) phase velocity of the wave front U = 20–100 m/s;
5) subsequent propagating waves are associated with the movement of the wave front.

During the period 2012−2015, using the "VISI" (Visible and near Infrared Spectral Imager) installed on the International Space Station, 306 mesospheric bore events were detected at latitudes between 55 ° N and 55 ° S in the airglow of molecular oxygen O_2 [Hozumi et al., 2019]. A classification of mesospheric bores was introduced based on their luminosity intensity relative to the background airglow of the O_2 layer, namely: bright bore and dark bore. Dark or bright bores appear depending on the height of the emission band relative to the MIL. If the bore propagates through the center inside a horizontal waveguide channel, the lower OH and Na layers are displaced downward and become bright, while the upper O_2 and [OI] layers are pushed upward, becoming dark. If the waveguide channel is located below the OH layer, the bore's airglow in this emission will be dark. The explanation of this effect and other examples are given in detail in the work [Medeiros et al., 2005], based on the results of studying 64 recorded mesospheric bore events over Brazil. Thanks to a rather large statistical database of mesospheric bores [Hozumi et al., 2019], seasonal distribution was revealed. The largest number of bores is observed in the winter hemisphere at the moments of solstices.

The aim of this work is to study the propagation features and formation mechanism of mesospheric bores based on data from all-sky cameras in the geographical conditions of Yakutia

territory. The results of the work are important for accumulating global statistics of these phenomena, which will help to clarify the causes of the formation of this phenomenon and their influence on the general circulation of the atmosphere.

2. EQUIPMENT AND DATA PROCESSING METHODOLOGY

Registration of wave processes in the airglow was carried out using digital all-sky cameras located at the Maimaga site (63.0 ° N, 129.5° E), located about ~130 km north of Yakutsk.

The first camera was created based on a CCD camera "ST-6" manufactured by Santa Barbara Instrument Group (USA). The camera uses a " fisheye " lens manufactured by Fisheye Nikkor (Japan) with a broadband glass filter " KS17 ", which transmits light in the near-infrared region of the spectrum (more than 660 nm), where the long-wavelength part of the spectrum (~1000 nm) is limited by the sensitivity drop of the recording receiver [Ammosov and Gavrilyeva, 2003]. In this range, mainly the bands of hydroxyl OH molecules are emitted, having a nominal emission height of 87 km. The camera has a resolution of 241x250 pixels. The horizontal resolution of a pixel at the zenith is about ~1 . 5 km. The interval between frames is 3 minutes with an exposure duration of 150 seconds.

The second all-sky camera is an improved version of the "ST-6" camera. It uses a CCD camera "ST-9" with a resolution of 512x512 pixels. The horizontal resolution of a pixel at the zenith is about ~0 . 7 km. The interval between frames is 1 minute with an exposure duration of 20 seconds.

The third all-sky camera "Keo Sentry" manufactured by Keo Scientific Ltd. (Canada) consists of a " fisheye " lens, a CCD camera "EMCCD PI Acton ProEM 1024B" and six interference filters [Ievenko and Parnikov, 2022]. In this work, a filter centered at the wavelength of 557.7 nm [OI] was used. The camera has a resolution of 1024x1024 pixels. The exposure duration is 10 seconds.

To better analyze data from all-sky camera images, the time differencing (TD) method is used [Swenson and Mende, 1994]. This method enhances changes occurring in emission intensity by pixel-by-pixel subtraction of two subsequent frames. In a wave structure with a wave period longer than the filming frequency, the brightness intensity after applying the TD method increases almost twofold, as the areas of wave maxima in the next frame occupy the areas of wave minima. For images with a filming frequency less than the period of wave disturbances, a modified TD method is applied, in which the resulting image is obtained from six consecutive frames. Data processing was carried out using a self-developed software package in the Python programming language

[Tyshchuk and Koltovskoy, 2023]. Observations were conducted during clear, moonless, geomagnetically quiet nights in the absence of visible forms of auroras.

In this study, measurements from MLS (Microwave Limb Sounder) aboard NASA's EOS Aura satellite are additionally used to obtain the temperature of the upper atmosphere. The Aura MLS temperature is extracted from bands near the spectral lines of O_2 at a frequency of 118 GHz. The vertical resolution is from 3 to 6 km. Spatial coverage ranges from 82 ° N to 82 ° S . The data were downloaded from (https://mls.jpl.nasa.gov/eos-aura-mls/index.php) version v.5.

Data from the SABER (Sounding of the Atmosphere using Broadband Emission Radiometry) instrument aboard NASA's TIMED (Thermosphere Ionosphere-Mesosphere-Energetics and Dynamics) satellite are also used to obtain information about instantaneous temperature during the night in the MLT (mesosphere and lower thermosphere) region. The SABER TIMED temperature is extracted from CO_2 emission channels. Vertical resolution is ~0 . 4 km. Spatial coverage alternates between the northern view (from 83 ° N to 52 ° S) and the southern view (latitude coverage from 52 ° S to 83 ° N). The data were downloaded from (https://saber.gats-inc.com/) version v2.0 level 2A.

3. OBTAINED RESULTS

The first mesospheric bore event was recorded by all-sky cameras on November 19, 2017. The wave front first appeared on the southeastern horizon at 13:49 UT and moved northwest. It reached the zenith of the all-sky camera at 14:22 UT. Smaller wave disturbances propagated sequentially behind the wave front. Figure 1 shows images of atmospheric airglow in the OH emission from the all-sky camera "ST-6".

Fig. 1.

The upper series of frames in Fig. 1 shows a clear wave front dividing the sky into light and dark areas. According to the classification by Hozumi et al. [2019], this front is a dark bore. The mesospheric bore propagated at an azimuth of 295 ° (northwest). To better visualize this wave event, differentiated images were obtained using the TD method, which are presented in the lower series of images in Fig. 1. The horizontal phase velocity of the mesospheric bore was calculated to be ~34 m/s. The observation time was 1 hour 18 minutes. Waves propagating sequentially behind the mesospheric bore were observed until 16:10 UT. Their wavelength is ~15 km. This wavelength value is characteristic of IGWs observed in various regions of the planet [Kim et al., 2010; Wrasse et al., 2024; Narayanan et al., 2024], including over the Maimaga site [Mordosova and Koltovskoy, 2022], where IGW wavelength values vary from ~7 to ~28 km with an average value of 16 km. The

phase velocity of the mesospheric bore and sequential IGWs corresponds to the permissible range (20-100 m/s). The propagation velocity values of gravity waves over the Maimaga site vary from ~10 to ~88 m/s with an average value of 35 m/s. In most other regions of the planet, the horizontal phase velocities of IGWs have the same values, with the exception of equatorial regions, where high phase velocities of IGWs are associated with low filtration of waves by weak winds in this region [Nakamura et al., 2003; Medeiros et al., 2004].

Fig. 2.

It is worth noting that on this day, in general, there was increased activity of wave disturbances, particularly IGWs. On November 19, 2017, four groups of IGWs were observed through the all-sky camera "ST-6" in the hydroxyl OH molecule emission, and three groups of IGWs were recorded by the all-sky camera "Keo Sentry" in the 557.7 nm [OI] emission. An interesting effect was observed in the [OI] line, where after the passage of the mesospheric bore, its successive wave disturbances were illuminated only in a limited area of the camera's zenith (Fig. 2). They were separated on both sides by a smaller group of IGWs propagating in the opposite direction (southeast). The movement of this effect can be better seen when viewing a video sequence of consecutive images.

Another mesospheric bore event was recorded on January 30, 2022, by the all-sky camera "ST-9". The wave front in the airglow emission first appeared on the northwestern horizon at 11:30 UT and spread to the southeast. It reached the zenith of the all-sky camera at 12:04 UT. Wave disturbances chained to the front move in the same direction. Figure 3 shows images of atmospheric airglow from the all-sky camera "ST-9" in the hydroxyl OH molecule emission.

Fig. 3.

A clear wave front dividing the sky into dark and light areas can be seen in the series of frames in Fig. 3. Unlike the previously considered event, the front is a bright bore. White arrows indicate the propagation direction of the mesospheric bore, which is 135 ° (southeast). The horizontal phase velocity of the mesospheric bore was calculated to be ~66 m/s. The observation time was 1 hour 23 minutes. After the bore left the horizon, the successively propagating waves ceased to be displayed in the airglow emission around 12:45 UT. The length of the successive IGWs is ~24 km. The parameters of the mesospheric bore and IGWs are different from the parameters of the first case described in this article. The propagation speed of the bright mesospheric bore and gravity waves is faster by 32 m/s, and the wavelength is greater by 9 km. This may be related to the propagation height of the mesospheric bore, the description of which will be in the next section.

4. DISCUSSION OF RESULTS

Using all-sky cameras located at the Maimaga test site, two mesospheric bore events were recorded on November 19, 2017, and January 30, 2022. These mesospheric bores meet the criteria of Loughmiller et al. [2007]. The primary criterion is the detection of a clearly distinguishable linear wave front that divides the atmospheric airglow into bright and dark regions, which is present in both of our cases. According to the classification by Hozumi et al. [2019], we identified two types of mesospheric bores: a dark bore on November 19, 2017, and a bright bore on January 30, 2022. Such different manifestations in the hydroxyl OH airglow emission indicate different heights of the horizontal waveguide channel through which the bores propagate. The first case of the dark bore phenomenon suggests that the channel is located below the OH layer, meaning the propagation height of the mesospheric bore is less than 87 km. To confirm this hypothesis, Aura MLS satellite data were analyzed. Knowing the bore propagation velocity and the time , required for its formation, it is possible to calculate the approximate radius of the bore formation area. In the presumed area along the direction of mesospheric bore movement, satellite measurements were conducted at three points, marked in Figure 4 *a* with a square. Observations at point 2737 were conducted at 18:47 UT (approximately ~1 hour after the bore passage at this point), at point 543 at 03:43 UT (about ~8 hours before the bore passage at this point), at point 2398 at 16:28 UT (about ~11 hours before the bore passage at this point). Figure 4 *b* shows the temperature profile of the upper atmosphere. To verify static stability, a vertical profile of the squared Brunt–Väisälä frequency was constructed, which is calculated using the formula

$$N^2 = \frac{g}{T\left(\Delta T_z + \frac{g}{C_p}\right)} N^2 = \frac{g}{T\left(\Delta T_z + \frac{g}{C_p}\right)}, \quad (1)$$

where g is the acceleration of gravity; T is temperature; ΔT_z is the vertical temperature gradient; C_p is the specific heat capacity at constant pressure. The value of N^2 at altitude z is obtained from two continuous Aura MLS temperature data points, and then the values in (1) take the form $T = (T(z_1) + T(z_2))/2$, $\Delta T_z = (T(z_2) - T(z_1))/(z_2 - z_1)$, $z = (z_1 + z_2)/2$.

At point 543 at the altitude of 69–88 km (Figure 4 *c*), an area with the highest value of N^2 (stable layer) is distinguished, surrounded by areas with low N^2 (unstable layers). This structure suggests the existence of a mesospheric inversion layer (MIL), which is a favorable condition for mesospheric bore propagation. At points 2737 and 2398, according to temperature data, there is no clear identification of the MIL structure, which suggests that the bore began to form approximately at the sea-land boundary.

The second event, where a bright bore was observed, implies that its waveguide channel is

located above the OH layer. It can be assumed that the bore propagated at altitudes between the emission layers of hydroxyl OH molecules and atomic oxygen [OI] molecules (87 and 96 km respectively). Information about the temperature in the MLT (mesosphere and lower thermosphere) region was obtained using satellite data from TIMED/SABER. The three nearest satellite observation points were selected along the direction of the bore movement, marked in Fig. 5 *a* with a square. Fig. 5 *b* shows the temperature profile of the MLT region. On the vertical profile of the Brunt-Väisälä frequency squared (N^2), a stable region is clearly distinguished above point 600 in the altitude range of 86-92 km (Fig. 5 *c*). This corresponds to the theory [Medeiros et al., 2005]. Above other measurement points, the MIL structure is not observed, so it can be assumed that the bore propagated past the zone of point 600, which probably means a slight change in the trajectory of movement over time.

Fig. 5.

The phase velocities of the wave fronts correspond to the permissible range U = 20-100 m/s. The horizontal phase velocity of bore propagation on November 19, 2017 was ~34 m/s, on January 30, 2022 ~66 m/s. The subsequent propagating waves were clearly associated with the movement of the front. They propagated along the same azimuthal direction but differed in their emission intensity from the bore. In the first event, the length of sequential IGWs behind the dark bore was ~15 km, and in the second event - behind the bright bore ~24 km.

The duration of observation of the mesospheric bore in the field of view of the all-sky camera is approximately the same and amounts to 1 h 18 min in the first case and 1 h 23 min in the second case.

Dewan and Picard [1998] suggested that the large wind shear formed by a temperature inversion layer may play an important role in the formation and propagation of mesospheric bores. Studies of the wind field over Xinlong (China) based on meteor radar data showed that the mean wind along the propagation direction of the mesospheric bore was weak at the OH height [Li et al., 2013]. However, during the bore passage, a strong background wind shear was observed in the 82-87 km altitude range. This confirmed that wind shear plays an important role in the formation of the mesospheric bore phenomenon.

The propagation of AGWs over the Maimaga site occurs predominantly in the northwestern direction [Mordosova and Koltovskoi, 2022]. It is known that AGWs are generated in the lower layers of the atmosphere (troposphere) and propagate upward through the middle atmosphere (stratosphere, mesosphere), undergoing the filtering effect of the jet stream [Nakamura et al., 1999]. In winter in the Northern Hemisphere, the background wind in the middle atmosphere is usually

directed from west to east. However, circulation dipoles (the relationship between cyclone and anticyclone) [Fritts and Nastrom, 1992] and orographic features of the area (mountain ranges, sea-land boundary) can contribute to the deviation of its direction. In addition to active meteorological processes in the troposphere (strong winds, hurricanes, etc.), the most important sources of AGW generation are wind shear (connection between jet stream and stratospheric polar vortex) [Wang et al., 2010] and atmospheric fronts (influence of humidity and temperature) [Waite and Snyder, 2012]. This has become a paradigm for studying waves in the jet exit region (JEREmi – Jet Exit Region Emission) [Plougonven and Zhang, 2014]. Most often, JEREmi waves are observed over mountain ranges, and less frequently over depressions. Their propagation is associated with the AGW enhancement mechanism through " wave trapping ," large-scale wave filtration and vertical wind shear.

According to the data from the Kamchatka Department for Hydrometeorology and Environmental Monitoring, on November 19, 2017, the Okhotsk Sea and Pacific Ocean waters were under the influence of a cyclone, and a storm warning was issued. This is confirmed by synoptic maps from the Arctic and Antarctic Research Institute (AARI) [Ivanov and Alekseenkov, 2021] and global wind and weather condition maps according to NCEP (National Centers for Environmental Prediction) data [Beccario, 2024]. A deep atmospheric cyclone (H) over the Okhotsk Sea (Fig. 6 *a*) is located in the presumed zone where the mesospheric bore begins to form.

Fig. 6.

At the geopotential height of 500 hPa (altitude ~5 km), the airflow of atmospheric vortices directed to the northwest formed a " step " (an area of sharp increase and decrease in wind speed) from and up to the possible collision with extended mountain ranges in the eastern part of Yakutia (Fig. 6 *b*). Such flowing of air around mountain massifs could form rotor disturbances [Kozhevnikov, 1999], which in turn, being subjected to the filtering effect of the jet stream, generate IGWs. The jet stream flow in the troposphere at a geopotential height of 250 hPa (altitude ~10 . 5 km) formed a curl (Fig. 6 *c*), probably caused by the deformation of the stratospheric polar vortex at a geopotential height of 70 hPa (altitude ~17.5 km) toward the equator (Fig. 6 *d*). After analyzing the available information, we assume that the source of the mesospheric bore generation on November 19, 2017, was the wind shear caused by the orographic features of the terrain.

In the second case, the area of mesospheric bore formation is larger than the first due to the higher horizontal phase velocity and propagation height. It is noteworthy that on January 30, 2022, a storm warning was also issued with reference to the Kaliningrad Center for Hydrometeorology and Environmental Monitoring. On this day, two strong North Atlantic cyclones were over the Kara and

Barents Seas (Fig. 7 *a*).

Fig. 7.

The movement of atmospheric vortices (Fig. 7 *b*) and jet streams (Fig. 7 *c*) deviates to the northeast before reaching Maymagy under the influence of an anticyclone (B) near the shores of the Laptev Sea. A slowdown of the polar vortex is observed near Maymagy (Fig. 7 *d*). Given the complex synoptic situation, it is difficult to determine the exact cause of the mesospheric bore occurrence on this day.

It is worth mentioning another event where the authors [Nikolashkin et al., 2024] managed to capture the phenomenon of a mesospheric bore in noctilucent clouds on July 28, 2002, also over Yakutia. The noctilucent clouds began to appear at 14:30 UT on the western horizon and gradually drifted eastward. At 14:45 UT, a front began to form, becoming more intense and spreading in length, occupying almost the entire sky. This front moved smoothly in the western direction, followed by a cloud field with less noticeable wave periodic structures. This combination in the structure of noctilucent clouds closely resembles the character of a mesospheric bore.

5. CONCLUSIONS

In this work, for the first time in domestic scientific literature, the features of the mesospheric bore phenomenon are described through observations of emission layer airglow with all-sky cameras. Two events observed at polar latitudes (63.0° N, 129.5° E) over the central part of Yakutia were identified.

The first event was recorded by two all-sky cameras in night sky airglow emissions on November 19, 2017. The bright mesospheric bore propagated from southeast to northwest (azimuth 295 °). The wave front in the hydroxyl OH airglow emission divided the sky into bright and dark areas. The observation time was 1 hour and 18 minutes. The horizontal phase velocity of the mesospheric bore was ~34 m/s. The length of consecutive IGWs was ~15 km. In the atomic oxygen [OI] airglow emission, IGWs were also observed, including those in the opposite direction relative to the waves following the bore. The presumed source of mesospheric bore generation was wind shear caused by orographic features of the terrain. Extended mountain ranges can cause rotor disturbances in air flows of atmospheric vortices, which, when subjected to the filtering effect of a jet stream, can form IGWs.

The second event was recorded by the all-sky camera on January 30, 2022, in the OH hydroxyl emission. The wavefront, as in the first case, divided the sky into light and dark areas. The dark mesospheric bore propagated from northwest to southeast (azimuth 135 º). The horizontal

phase velocity of the mesospheric bore was ~66 m/s. The observation time was 1 hour 23 minutes. The length of the consecutive IGWs was ~24 km. After the bore disappeared over the horizon, the consecutively propagating waves ceased to appear in the emission glow. It is difficult to determine the exact cause of the mesospheric bore generation on this day.

FUNDING

The work was carried out within the framework of State Assignment No. 122011700172-2.

REFERENCES

– *Ivanov V.V., Alekseenkov G.A.* Surface and upper-air meteorological maps. ODMP AANII. 2021. https://www.aari.ru/data/realtime

– *Ievenko I.B., Parnikov S.G.* Relationship between SAR-arc dynamics and substorm injection according to aurora observations. Magnetospheric phenomena in the vicinity of the plasmapause // Geomagnetism and Aeronomy. Vol. 62. No. 2. P. 171 − 188. 2022. doi 10.31857/S0016794022020092

– *Kozhevnikov V.N.* Atmospheric disturbances during mountain flow. Moscow: Scientific World, 160 p. 1999.

– *Mordosova O.V., Koltovskoy I.I.* Investigation of internal gravity waves using an infrared all-sky camera over the territory of Yakutia // Bulletin of KRAUNC. Physical & Mathematical Sciences. Vol. 40. No. 3. P. 227 − 238. 2022. https://doi.org/10.26117/2079-6641-2022-40-3-227-238

– *Nikolashkin S.V., Koltovskoy I.I., Ammosova A.M.* Features of the mesosphere wave structure from noctilucent clouds observations // Atmospheric and Oceanic Optics. Vol. 37. No. 5. P. 403 − 408. 2024. https://doi.org/10.15372/AOO20240507

– *Saveliev I.V.* Course of general physics. Vol. 1. Mechanics, oscillations and waves, molecular physics. Moscow: Nauka, 263 p. 1970.

– *Tricker R.* Bore, surf, swell and ship waves. Leningrad: Gidrometeoizdat, 286 p. 1969.

– *Tyshchuk O.V., Koltovskoy I.I.* Development of a program for processing and analyzing all-sky camera data in Python / Materials of the scientific conf. of students, postgraduates and young scientists of the XXV Lavrentiev Readings of the Republic of Sakha (Yakutia). Yakutsk, 10 − 13 April 2023. Yakutsk: NEFU Publishing House. P. 82−85. 2023.

– *Ammosov P.P., Gavrilyeva G.A.* Observations of short-term waves with an all sky camera in the infrared oh brightness over Yakutsk / Physics of Auroral Phenomena: Proc. XXVI Annual Seminar. Apatity, 15-18 February 2003. P. 179−181. 2003.

– *Beccario C.* Earth: a visualization of global weather conditions. 2024. https://earth.nullschool.net
– *Dewan E.M., Picard R.H.* Mesospheric bores // J. Geophys. Res. – Atmos. V. 103. N 6. P. 6295−6305. 1998. https://doi.org/10.1029/97JD02498
– *Dewan E.M., Picard R.H.* On the origin of mesospheric bores // J. Geophys. Res. – Atmos. V. 106. N 3. P. 2921−2927. 2001. https://doi.org/10.1029/2000JD900697
– *Fritts D.C., Nastrom G.D.* Sources of mesoscale variability of gravity waves. Part II: Frontal, convective, and jet stream excitation // J. Atmos. Sci. V. 49. N 2. P. 111−127. 1992. https://doi.org/10.1175/1520-0469(1992)049<0111:SOMVOG>2.0.CO;2
– *Hozumi Y., Saito A., Sakanoi T., Yamazaki A., Hosokawa K., Nakamura T.* Geographical and seasonal variability of mesospheric bores observed from the International Space Station // J. Geophys. Res.− Space. V. 124. N 5. P. 3775−3785. 2019. https://doi.org/10.1029/2019JA026635
– *Kim Y.H., Lee C.S., Chung J.K., Kim J.H., Chun H.Y.* Seasonal Variations of Mesospheric Gravity Waves Observed with an Airglow All-sky Camera at Mt. Bohyun, Korea (36°N) // J. Astron. Space Sci. V. 27. N 3. P. 181−188. 2010. https://doi.org/10.5140/JASS.2010.27.3.181
– *Li Q., Xu J., Yue J., Liu X., Yuan W., Ning B., Guan S., Younger J. P.* Investigation of a mesospheric bore event over northern China // Ann. Geophys. V. 31. N 3. P. 409−418. 2013. https://doi.org/10.5194/angeo-31-409-2013
– *Loughmiller P.J., Kelley M.C., Hickey M.P., Picard R.H., Wintersteiner P.P., Winick J.R., Dewan E.M.* Observational and modeling study of mesospheric bores / Proceedings Advanced Maui Optical and Space Surveillance Technologies (AMOS) Technologies Conference. Wailea, Hawaii, 12−15 September 2007. 2007.
– *Medeiros A.F., Buriti R.A., Machado E.A., Takahashi H., Batista P.P., Gobbi D., Taylor M.J.* Comparison of gravity wave activity observed by airglow imaging from two different latitudes in Brazil // J. Atmos. Sol-Terr. Phy. V. 60. N 6–9. P. 647−654. 2004. https://doi.org/10.1016/j.jastp.2004.01.016
– *Medeiros A.F., Fechine J., Buriti R.A., Takahashi H., Wrasse C.M., Gobbi D.* Response of OH, O_2 and OI5577 airglow emissions to the mesospheric bore in the equatorial region of Brazil // Adv. Space Res. V. 35 N 11. P. 1971−1975. 2005. https://doi.org/10.1016/j.asr.2005.03.075
– *Nakamura T., Higashikawa A., Tsuda T., Matsushita Y.* Seasonal variations of gravity wave structures in OH airglow with a CCD imager at Shigaraki // Earth Planets Space. V. 51. N 7−8. P. 897−906. 1999. https://doi.org/10.1186/BF03353248
– *Nakamura T., Aono T., Tsuda T., Admiranto A.G, Achmad E., Suranto.* Mesospheric gravity waves over a tropical convective region observed by OH airglow imaging in Indonesia // Geophys. Res.

Lett. V. 30. N 17. ID 1882. 2003. https://doi.org/10.1029/2003GL017619

– *Narayanan V.L., Wright C.J., Mlynczak M.G., Hindley N., Kavanagh A.J., Moffat-Griffin T., Noble P.* Observations of mesospheric gravity waves generated by geomagnetic activity // J. Geophys. Res. − Space. V. 129. N 4. ID e2023JA032157. 2024. https://doi.org/10.1029/2023JA032157

– *Plougonven R., Zhang F.* Internal gravity waves from atmospheric jets and fronts // Rev. Geophys. V. 52. N 1. P. 33−76. 2014. https://doi.org/10.1002/2012RG000419

– *Stoker J.J.* The formation of breakers and bores. The theory of nonlinear wave propagation in shallow water and open channels // Commun. Pur. Appl. Math. V. 1. N 1. P. 1−87. 1948. https://doi.org/10.1002/cpa.3160010101

– *Swenson G.R., Mende S.B.* OH emission and gravity wave (including a breaking wave) in all-sky imagery from Bear Lake // Geophys. Res. Lett. V. 21. N 20. P. 2239−2242. 1994. https://doi.org/10.1029/94GL02112

– *Taylor M.J., Turnbull D.N., Lowe R.P.* Spectrometric and imaging measurements of a spectacular gravity wave event observed during the ALOHA-93 campaign // Geophys. Res. Lett. V. 22. N 20. P. 2849−2852. 1995. https://doi.org/10.1029/95GL02948

– *Waite M.L., Snyder C.* Mesoscale energy spectra of moist baroclinic waves // J. Atmos. Sci. V. 70. N 4. P. 1242−1256. 2012. https://doi.org/10.1175/JAS-D-11-0347.1

– *Walterscheid R.L., Hecht J.H., Gelinas L.J., Hickey M.P., Reid I.M.* An intense traveling airglow front in the upper mesosphere–lower thermosphere with characteristics of a bore observed over Alice Springs, Australia, during a strong 2 day wave episode // J. Geophys. Res. – Atmos. V. 117. N 22. ID D22105. 2012. https://doi.org/10.1029/2012JD017847

– *Wang S., Zhang F., Epifanio C.C.* Forced gravity wave response near the jet exit region in a linear model // Q. J. R. Meteor. Soc. V. 136. N 652. P. 1773−1787. 2010. https://doi.org/10.1002/qj.676

– *Wrasse C.M., Nyassor P.K., da Silva L.A., Figueiredo C.A.O.B., Bageston J.V., Naccarato K.P., Barros D., Takahashi H., Gobbi D.* Studies on the propagation dynamics and source mechanism of quasi-monochromatic gravity waves observed over São Martinho da Serra (29° S, 53° W), Brazil // Atmos. Chem. Phys. V. 24. N 9. P. 5405−5431. 2024. https://doi.org/10.5194/acp-24-5405-2024

Figure Captions

Fig. 1. Images in OH emission from the "ST-6" all-sky camera, showing the movement of the mesospheric bore on November 19, 2017, at 13:49 UT (bore appearance), 14:22 UT (bore at the camera's zenith), and 14:49 UT (bore leaving the camera's field of view). The upper frames show the OH airglow images. The dark mesospheric bore and its propagation direction are indicated by black arrows. The lower frames show TD images. The images have a mirror reflection, and the compass in the upper right corner indicates the cardinal directions (the north direction is shifted 10° clockwise).

Fig. 2. Images obtained by the TD method in [OI] emission from the "Keo Sentry" all-sky camera on November 19, 2017, showing the propagation of two oppositely directed IGW groups. The black arrow indicates the directions of wave disturbances, the white dashed line shows the boundary between them.

Fig. 3. Images in OH emission from the "ST-9" all-sky camera, showing the movement of a mesospheric bore on January 30, 2022 at 11:40 UT (bore appearance), 12:04 UT (bore at camera zenith) and 12:23 UT (leaving the camera field of view). The bright mesospheric bore and its propagation direction are indicated by white arrows.

Fig. 4. Aura MLS data on November 19, 2017. (*a*) – satellite measurement points in the presumed bore propagation area are marked with a square, the Maimaga polygon is marked with an asterisk, the arrow indicates the direction of the mesospheric bore movement; (*b*) – vertical temperature profile of the upper atmosphere; (*c*) – vertical profile of the Brunt-Väisälä frequency.

Fig. 5. SABER TIMED data on January 30, 2022. (*a*) – satellite measurement points are marked with a square, the Maimaga polygon is marked with an asterisk, the arrow indicates the mesospheric bore propagation direction; (*b*) – vertical temperature profile of the MLT region; (*c*) – vertical profile of the Brunt-Väisälä frequency.

Fig. 6. Global wind map on November 19, 2017 at 12:00 UT at various geopotential heights (700 hPa, 500 hPa, 250 hPa, 70 hPa) [Beccario, 2024]. The Maimaga polygon is marked with an asterisk.

H – cyclone areas. Arrows serve as indicators of airflow direction. The presumed formation area of the mesospheric bore is highlighted with a frame.

Fig. 7. Global wind map on January 30, 2022 at 11:00 UT at various geopotential heights (700 hPa, 500 hPa, 250 hPa, 70 hPa) [Beccario, 2024]. Designations as in Fig. 6.

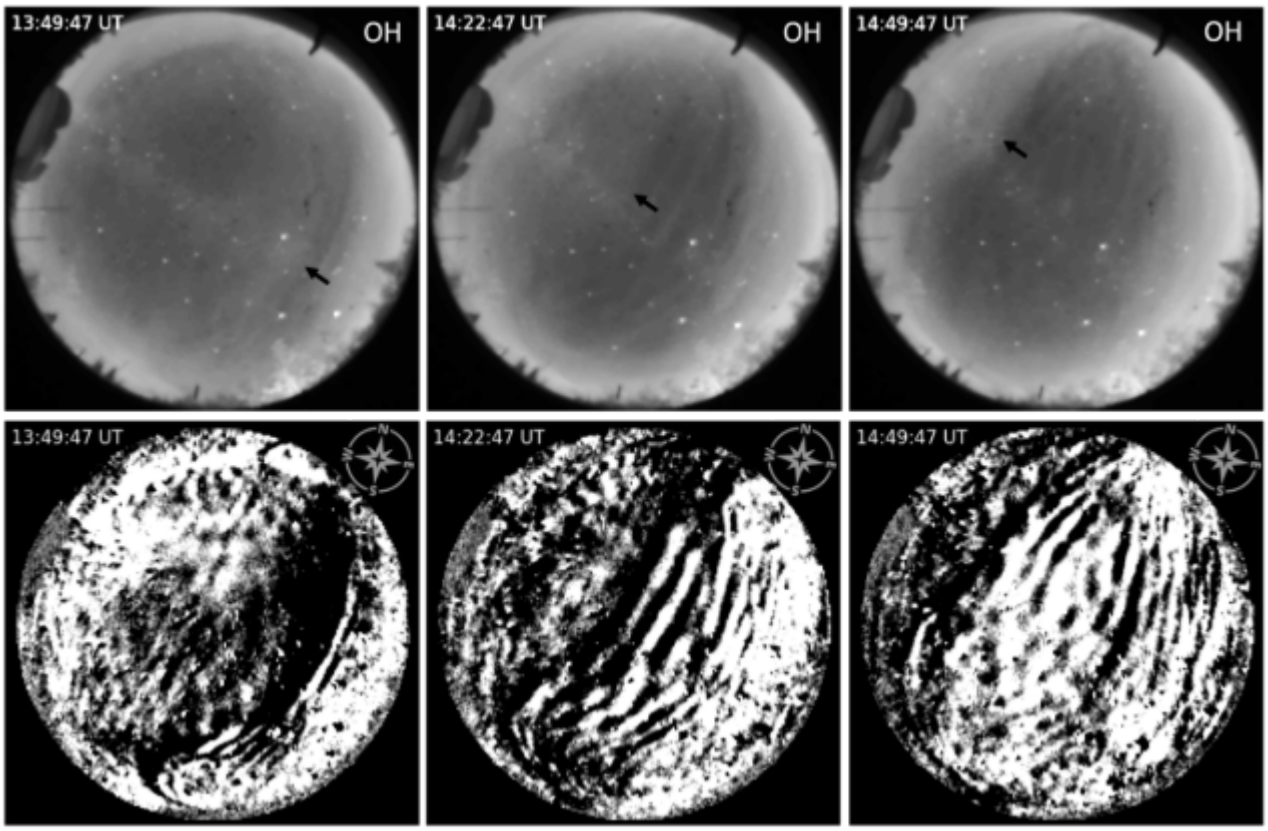

Fig. 1.

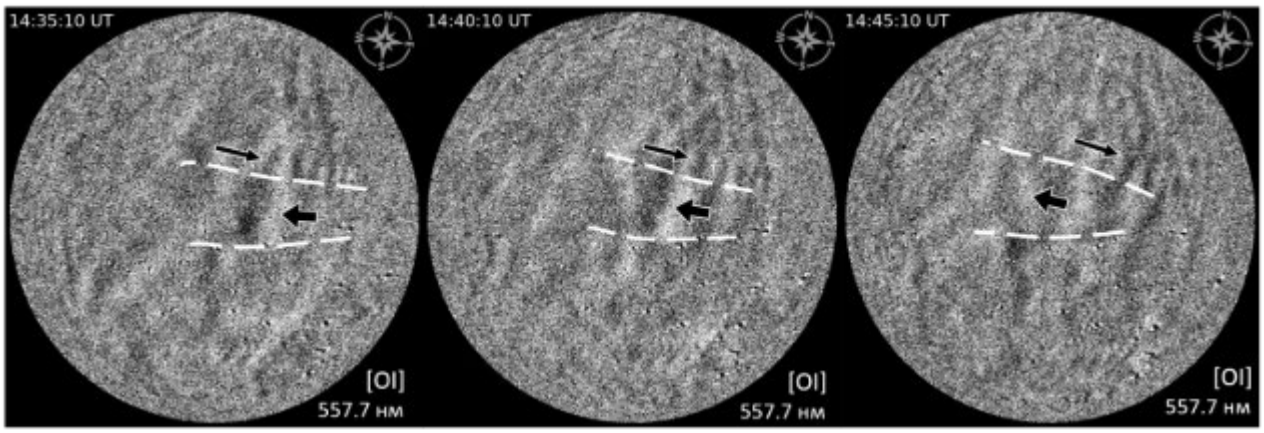
14:35:10 UT
14:40:10 UT
14:45:10 UT
[OI]
557.7 нм
[OI]
557.7 нм
[OI]
557.7 нм

Fig. 2.

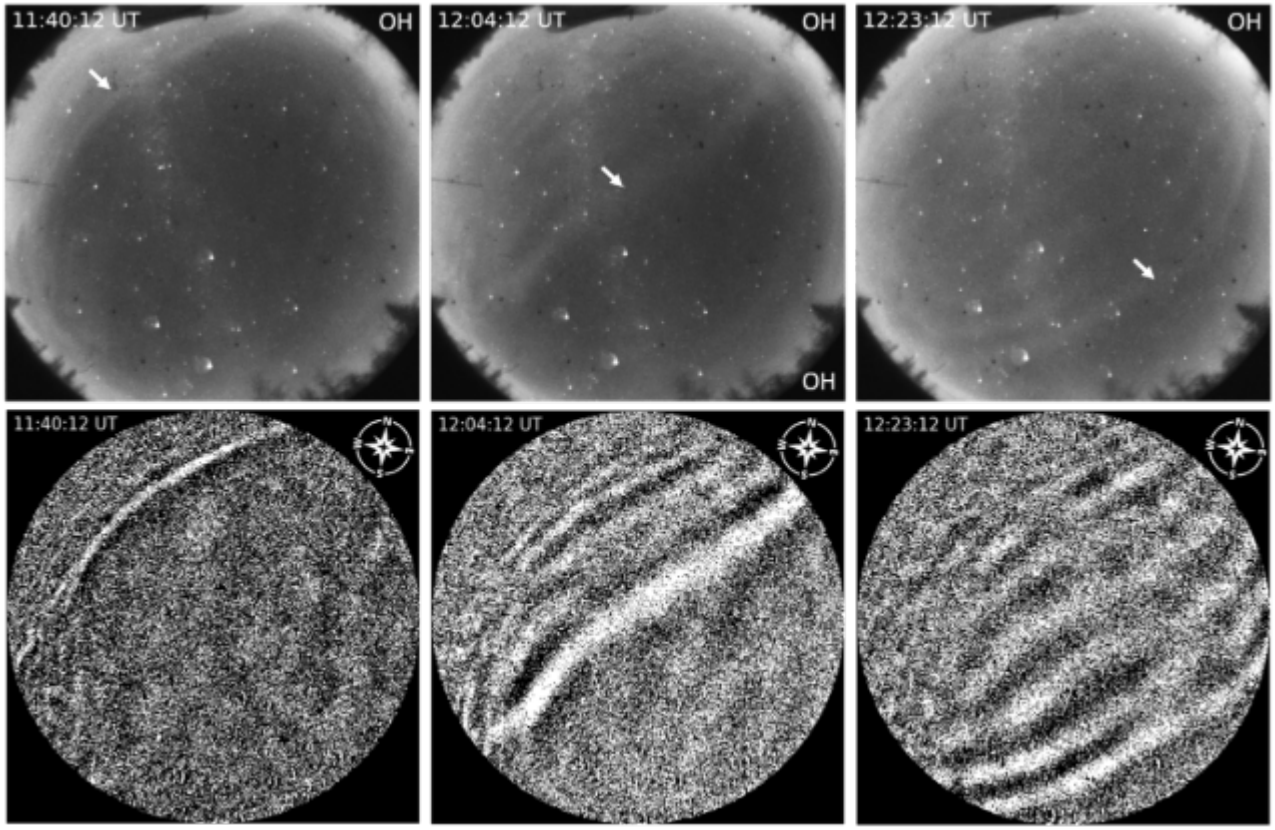
11:40:12 UT
OH
12:04:12 UT
OH
12:23:12 UT
OH
OH
11:40:12 UT
12:04:12 UT
12:23:12 UT

Fig. 3.

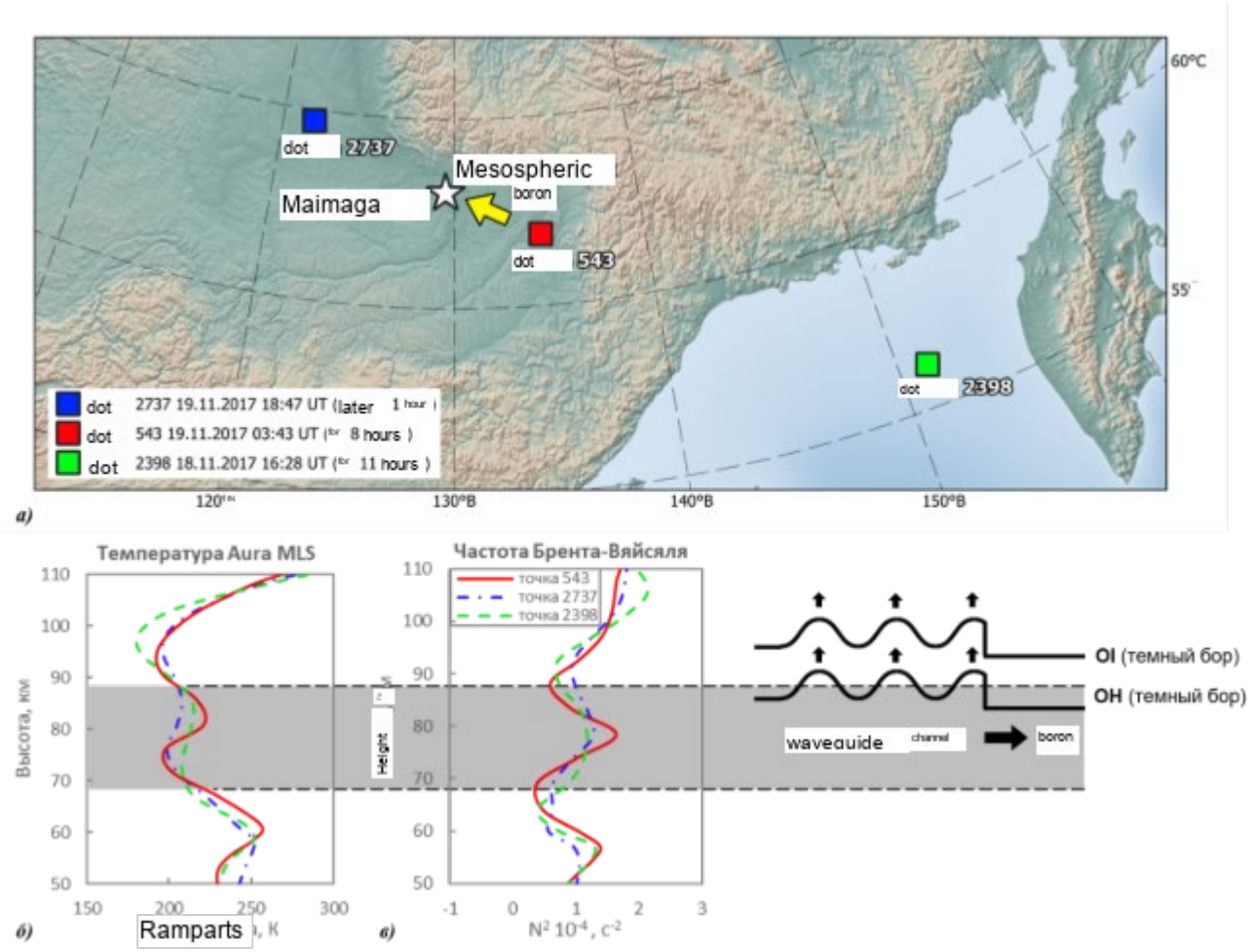
dot 2737
Mesospheric
Maimaga
boron
dot 543
dot 2398
60°C
55°
dot 2737 19.11.2017 18:47 UT (later 1 hour)
dot 543 19.11.2017 03:43 UT (by 8 hours)
dot 2398 18.11.2017 16:28 UT (by 11 hours)
120°W
130°B
140°B
150°B
а)
Температура Aura MLS
Высота, км
Ramparts
б)
Частота Брента-Вяйсяля
точка 543
точка 2737
точка 2398
Height
N² 10⁻⁴, c⁻²
в)
OI (темный бор)
OH (темный бор)
waveguide
channel
boron

Fig. 4.

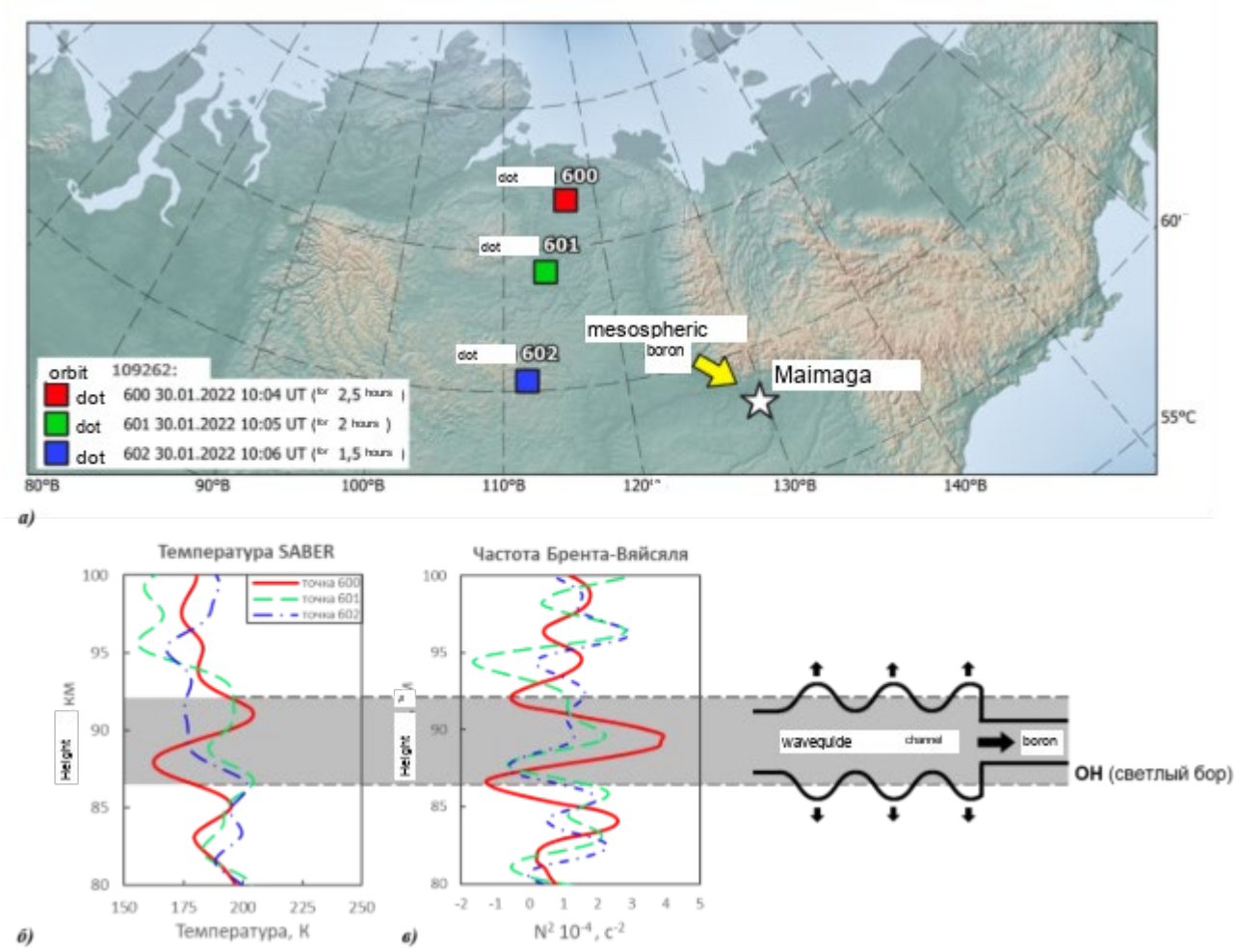
dot
600
dot
601
dot
602
mesospheric
boron
Maimaga
orbit 109262:
dot 600 30.01.2022 10:04 UT (for 2,5 hours)
dot 601 30.01.2022 10:05 UT (for 2 hours)
dot 602 30.01.2022 10:06 UT (for 1,5 hours)
80°B
90°B
100°B
110°B
130°B
140°B
60°
55°C
а)
Температура SABER
точка 600
точка 601
точка 602
Height, KM
Температура, K
б)
Частота Брента-Вяйсяля
Height, K
N² 10⁻⁴, c⁻²
в)
waveguide
channel
boron
OH (светлый бор)

Fig. 5.

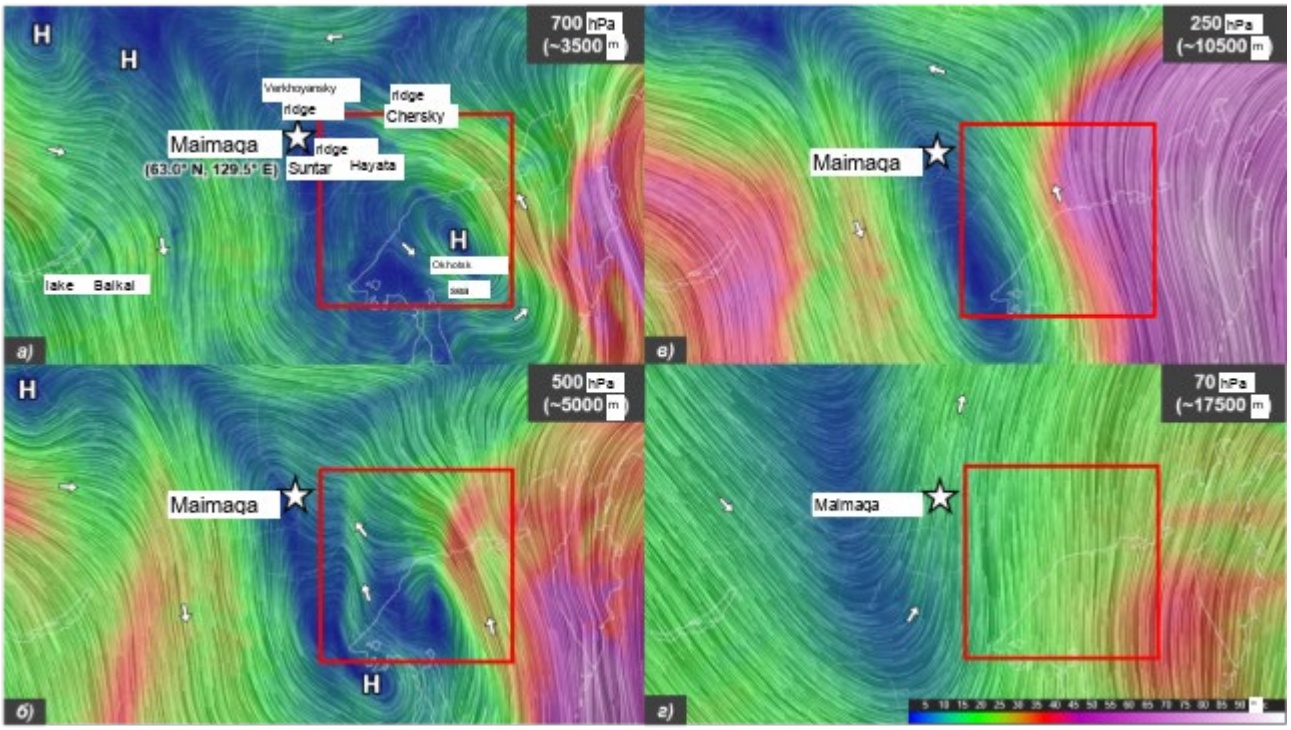
700 hPa
(~3500 m)
250 hPa
(~10500 m)
500 hPa
(~5000 m)
70 hPa
(~17500 m)
Maimaqa
(63.0° N, 129.5° E)
Verkhoyansky
ridge
ridge
Chersky
ridge
Suntar
Hayata
Okhotsk
sea
lake Baikal
а)
в)
б)
г)

Fig. 6.

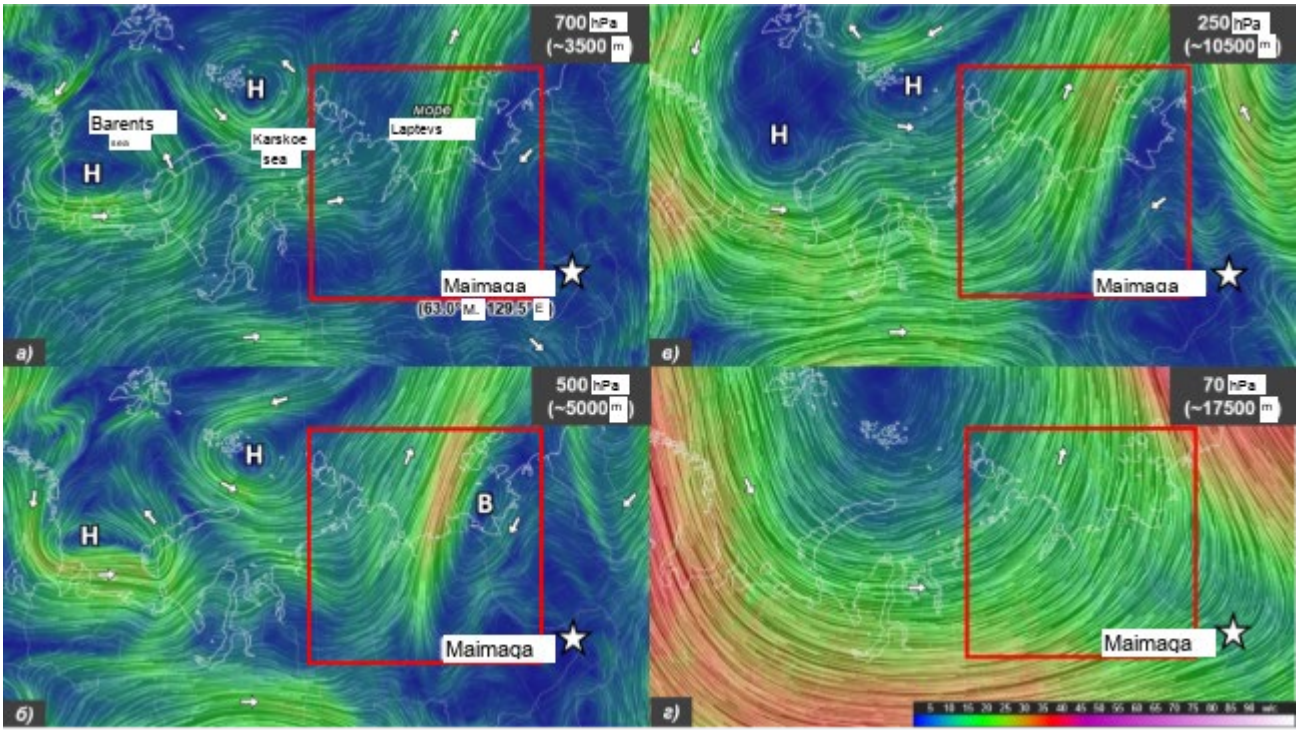
700 hPa
(~3500 m)
250 hPa
(~10500 m)
500 hPa
(~5000 m)
70 hPa
(~17500 m)
Barents
sea
Karskoe
sea
Море
Laptevs
Maimaqa
(63.0° N, 129.5° E)
а)
в)
б)
г)

Fig. 7.